JOURNAL OF GUIDANCE, CONTROL, AND DYNAMICS
Vol. 18, No. 2, March–April 1995

Dynamics and Control of Limit Cycling Motions in Boosting Rockets

Brett Newman*
Old Dominion University, Norfolk, Virginia 23529-0247

An investigation concerning the prediction and control of observed limit cycling behavior in a boosting rocket is considered. The suspected source of the nonlinear behavior is the presence of Coulomb friction in the nozzle pivot mechanism. A classical sinusoidal describing function analysis is used to accurately recreate and predict the observed oscillatory characteristic. From this analysis, insight is offered into the limit cycling mechanism and confidence is gained in the closed-loop system design. Nonlinear simulation is used to support and verify the results obtained from describing function theory. Insight into the limit cycling behavior is, in turn, used to adjust control system parameters to indirectly control the oscillatory tendencies. Tradeoffs with the guidance and control system stability/performance are also noted. Finally, active control of the limit cycling behavior, using a novel feedback algorithm to adjust the inherent nozzle sticking–unsticking characteristics, is considered.

Introduction

THE ballistic tactical target vehicle (BTTV) is a suborbital rocket whose re-entry vehicle serves as a target for advanced air defense and theater defense systems under development.[1,2] Flight telemetry results from the first two missions indicate the presence of low-amplitude, low-frequency steady oscillations in both the vehicle attitude and actuator piston displacement.[3,4] Figure 1 illustrates this characteristic in the vehicle pitch attitude response during second stage boost of the first mission. Note the flight data has been post processed. The impact of the oscillatory motions on the guidance and control objectives appear to have been minor; however, their presence was unexpected and is of concern, especially with regards concerning the origins of the oscillatory behavior and the physical mechanism by which they occur.

The hardware in question is the decommissioned Minuteman I Stage 3 system which is used as the second stage for the BTTV vehicle. After discussions with individuals intimately familiar with the Minuteman I Stage 3 characteristics, it became known that this system has a long history of exhibiting small, slow periodic motions during the boost phase. These characteristics are, in fact, so common that routine preflight analysis is used in estimating the oscillatory motion for the specific flight vehicle/control system in question. The results are then compared with an existing database to determine whether the oscillatory motions will impact the guidance and control mission objectives. This database suggests the oscillatory motions are limit cycling behavior due to nonlinearities present in the actuator-nozzle system, a conventional hydraulic actuator driving vectorable nozzles. Coulomb or dry friction present in the nozzle pivot is the primary culprit. Additional nonlinearities are present but are not considered here.

The first goal of this research is to provide an accurate prediction, if possible, of the oscillatory behavior experienced by the BTTV flight vehicle.[5] This analysis should provide insight as to the origin of and the mechanism by which the characteristics occur. Sinusoidal describing function theory and nonlinear simulation are to be employed in achieving this goal. A second goal of this research is to explore means by which the oscillatory motions may be controlled to lessen the impact upon the guidance and control performance.[5] The implemented control systems should also have minimal impact on the performance of the guidance and control feedback loops, while simultaneously providing sufficient robustness against reasonably expected modeling uncertainties and errors. Feedback gain adjustment and a novel impulsive control approach are considered.

Received Aug. 3, 1993; revision received Aug. 15, 1994; accepted for publication Aug. 15, 1994.

*Assistant Professor, Department of Aerospace Engineering. Member AIAA.

System Modeling

The small perturbation dynamics of the longitudinal axis of the BTTV vehicle are governed by the guidance and control loops illustrated in Fig. 2.[6,7] In Fig. 2, the inner and outer loops provide proportional plus derivative control of the attitude and translational modes by feeding back pitch angle θ and position x. Here, x_c represents the commanded position, G_i and G_o denote the inner and outer loop vehicle transfer functions, and K_s, K_r, K_p, and K_d are the feedback gains. The feedback structure gives rise to the commanded nozzle deflection δ_c which serves as the input to the actuator-nozzle transfer function $G_{a/n}$. Nozzle deflection δ is the response of this block and serves as the control input to the vehicle.

A typical point along the flight trajectory during the Minuteman I Stage 3 burn occurs 70 s after first stage ignition. The altitude at this point is sufficiently high that aerodynamic loads acting on the vehicle can be neglected. In this case, simple transfer function models for G_i and G_o are[6]

$$G_i(s) = [(l_v T_v)/I_v]/s^2, \qquad G_o(s) = (T_v/m_v)/s^2 \tag{1}$$

where l_v is the control moment arm, m_v the vehicle mass, I_v the vehicle moment of inertia, and T_v the control thrust. The following numerical values are taken from Ref. 6 at 70 s into the mission:

$$l_v = 8.491 \text{ ft} \qquad I_v = 7280 \text{ slug ft}^2 \qquad m_v = 165.8 \text{ slug}$$
$$T_v = 9854 \text{ lbf} \qquad K_s = 0.88 \qquad K_r = 0.4 \text{ s} \tag{2}$$
$$K_p = 0.000363 \text{ 1/ft} \qquad K_d = 0.00363 \text{ s/ft}$$

To investigate limit cycling behavior due to the nonlinear characteristics present in the actuator-nozzle system, a detailed model of the internal features of this subsystem is required, especially with regard to the nozzle where the suspect nonlinearity is present. Figure 3 illustrates a simple hydraulic actuator system. Input displacement to the actuator d_i causes fluid flow q_1 from the high-pressure supply to displace the actuator output piston d_o, whereas fluid on the opposite side is allowed to escape through the low pressure drain q_2. As a result of the inherent k/s dynamics, the output displacement is servoed with a feedback loop using the commanded nozzle deflection δ_c. Parameters of interest are fluid density ρ, piston area A, piston mass m, driving pressure P_1, back pressure P_2, feedback gain K_a, and angular to linear conversion gain a.

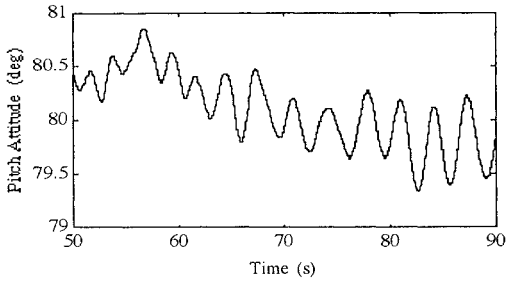

Fig. 1 Pitch attitude response during flight.

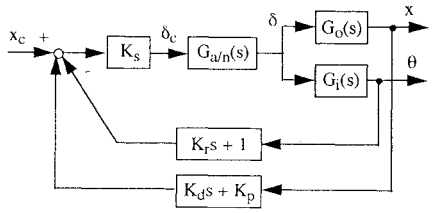

Fig. 2 Vehicle guidance and control loops.

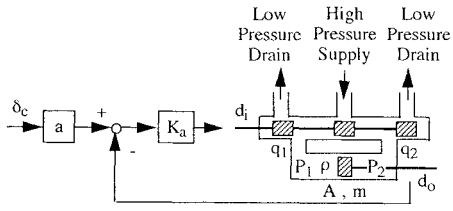

Fig. 3 Simple hydraulic actuator model.

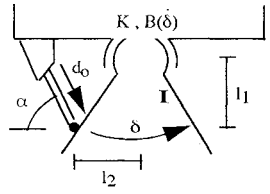

Fig. 4 Simple nozzle model.

Using basic principles from mechanics, feedback control, and hydraulics yields

$$\begin{aligned} (P_1 - P_2)A - T &= m\ddot{d}_o, \qquad q_1 = A\rho\dot{d}_o = q_2 \\ d_i &= K_a(a\delta_c - d_o) \\ q_1 &= K_{1_{d_i}} d_i - K_{p_1} P_1, \qquad q_2 = K_{2_{d_i}} d_i + K_{p_2} P_2 \end{aligned} \tag{3}$$

Using Eq. (3), the governing relationship between the output displacement and the commanded nozzle deflection is

$$\{m\}\ddot{d}_o + \left\{A^2\rho\left(\frac{1}{K_{p_1}} + \frac{1}{K_{p_2}}\right)\right\}\dot{d}_o + \left\{A\left(\frac{K_{1_{d_i}}}{K_{p_1}} + \frac{K_{2_{d_i}}}{K_{p_2}}\right)K_a\right\}d_o$$

$$= \left\{A\left(\frac{K_{1_{d_i}}}{K_{p_1}} + \frac{K_{2_{d_i}}}{K_{p_2}}\right)K_a a\right\}\delta_c - T \tag{4}$$

In Eq. (4), T denotes the load from the nozzle and represents coupling to the nozzle dynamics, which is addressed next.

Figure 4 illustrates the nozzle arrangement. Parameters of interest are the nozzle pivot to piston attachment length l_1, nozzle centerline to piston attachment length l_2, piston axis angle α, nozzle spring coefficient K, nozzle damping torque $B(\dot{\delta})$, and nozzle inertia I. The governing equation for the nozzle deflection due to the applied load T from the actuator is

$$-B(\dot{\delta}) - K\delta + bT = I\ddot{\delta} \tag{5}$$

where $b = l_1\cos(\alpha) + l_2\sin(\alpha)$. Again, note the coupling between the actuator and nozzle.

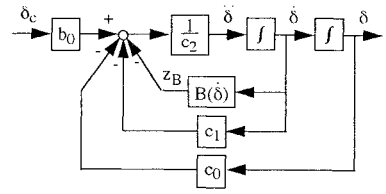

Fig. 5 Actuator-nozzle block diagram.

The overall actuator-nozzle model can now be had by eliminating T from Eqs. (4) and (5) and noting that $d_o = \{l_1/\cos(\alpha)\}\delta = a\delta$. The result is

$$\begin{aligned} c_2\ddot{\delta} + \{B(\dot{\delta}) + c_1\dot{\delta}\} + c_0\delta &= b_0\delta_c \\ b_0 &= A\left(\frac{K_{1_{d_i}}}{K_{p_1}} + \frac{K_{2_{d_i}}}{K_{p_2}}\right)K_a ab \\ c_0 &= K + A\left(\frac{K_{1_{d_i}}}{K_{p_1}} + \frac{K_{2_{d_i}}}{K_{p_2}}\right)K_a ab \\ c_1 &= A^2\rho\left(\frac{1}{K_{p_1}} + \frac{1}{K_{p_2}}\right)ab \qquad c_2 = I + mab \end{aligned} \tag{6}$$

This relationship is further depicted in block diagram form in Fig. 5. Finally, the damping torque $B(\dot{\delta})$ in Eq. (6) and Fig. 5 represents the nonlinearity suspected as the genesis of the limit cycling behavior, i.e., Coulomb friction or $B(\dot{\delta}) = f\,\mathrm{sgn}\{\dot{\delta}\}$ where f denotes the constant friction torque level.

Numerical data for the actuator-nozzle system originated from various sources.[8–11] The values are

$$\begin{aligned} &m = 0.1553 \text{ slug} \qquad I = 0.7333 \text{ slug ft}^2 \qquad A = 0.004630 \text{ ft}^2 \\ &l_1 = 0.4167 \text{ ft} \qquad l_2 = 0.625 \text{ ft} \qquad \rho = 1.553 \text{ slug/ft}^3 \\ &\alpha = 55 \text{ deg} \qquad f = 137.5 \text{ lbf ft} \qquad K = 691.7 \text{ (lbf ft)/rad} \\ &K_{1_{d_i}} K_a = K_{2_{d_i}} K_a = 0.6188 \text{ slug/(ft s)} \\ &K_{p_1} = K_{p_2} = 6.241 \times 10^{-8} \text{ ft s} \end{aligned} \tag{7}$$

Limit Cycling Prediction

Observe that for the given, isolated actuator-nozzle model in Eq. (6) or Fig. 5, no limit cycling can occur due to Coulomb friction.[12–14] To illustrate this fact, consider the response to an initial condition in the nozzle deflection as shown in Fig. 6. From Eq. (6), the governing equation of motion for segments 1–2 and 2–3, for example, are

$$\begin{aligned} c_2\ddot{\delta} + c_1\dot{\delta} + c_0\delta &= f \qquad \text{for} \qquad 1\text{–}2\ (\dot{\delta} < 0) \\ c_2\ddot{\delta} + c_1\dot{\delta} + c_0\delta &= -f \qquad \text{for} \qquad 2\text{–}3\ (\dot{\delta} > 0) \end{aligned} \tag{8}$$

The piecewise linear responses in Fig. 6 consist of exponentially decaying, sinusoidal oscillations, that are offset from zero by $\pm f/c_0$. The Coulomb damping manifests itself by offsetting each segmented response, thus reducing the peak overshoot value that would otherwise occur. These oscillations continue until the peak overshoot lies within the $\pm f/c_0$ band, at which time the spring torque is no longer sufficient to overcome the Coulomb friction torque, and the nozzle comes to rest at a nonzero value. This type of motion can not exhibit limit cycling behavior.

The actuator-nozzle system is not an isolated element, but rather is located within a feedback loop, as evidenced by substituting the block diagram in Fig. 5 into the appropriate location in the guidance and control feedback loops in Fig. 2. Therefore, for the given actuator-nozzle model in Eq. (8), if any limit cycling tendency is to occur, it comes from the coupling between the vehicle dynamics and the actuator-nozzle dynamics via feedback.

The mechanism for the limit cycling behavior is the following.[12–14] Suppose, as in Fig. 2, the guidance and control loops give rise to a commanded nozzle deflection signal. As just shown, the nozzle will stick at a value near, but not quite equal to, the commanded value. As the attitude and position respond to the nozzle

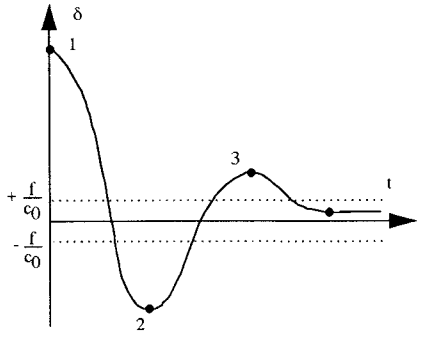

Fig. 6 Initial condition response for isolated actuator-nozzle system.

input, their values are fed back around the loop into the commanded nozzle deflection. When sufficiently large, the commanded signal overcomes the Coulomb friction torque and the nozzle unsticks, only to later stick near, but not equal to, the new commanded value. In this manner, the vehicle and actuator-nozzle tend to oscillate.

To predict the limit cycling behavior, sinusoidal describing function theory is employed.[12,14–16] The first task is to develop the describing function N and remnant r for Coulomb friction. For an input signal to $B(\dot{\delta})$ of

$$\dot{\delta} = A_{\dot{\delta}} \sin(\omega t) \tag{9}$$

the output signal is given as

$$z_B = \frac{4f}{\pi}\left[\sin(\omega t) + \frac{\sin(3\omega t)}{3} + \frac{\sin(5\omega t)}{5} + \cdots\right] \tag{10}$$

From Eq. (10), the describing function and remnant are calculated as[12]

$$N(A_{\dot{\delta}}) = \frac{4f}{\pi A_{\dot{\delta}}}, \qquad r = \frac{4f}{\pi}\left[\frac{\sin(3\omega t)}{3} + \frac{\sin(5\omega t)}{5} + \cdots\right] \tag{11}$$

An assumption here is that all of the linear elements wrapped around $B(\dot{\delta})$ provide sufficient attenuation such that the effect of the remnant as it travels around the loop to the input to N is negligible and, thus, $B(\dot{\delta})$ can be replaced by N. The validity of this step is addressed later. The second task is to develop the expression for the output signal z_B for the vehicle actuator-nozzle closed-loop system depicted in Figs. 2 and 5 with $B(\dot{\delta})$ replaced by N. The desired expression is

$$P(s)z_B = Q(s)x_c$$

$$P(s) = 1 + \frac{c_1}{c_2 s} + \frac{c_0 + b_0 K_s\{(K_r s + 1)G_i + (K_d s + K_p)G_o\}}{c_2 s^2} + \frac{N}{c_2 s} \tag{12}$$

For a zero position command ($x_c = 0$), the condition for limit cycling to exist is that the coefficient $P(s)$ in Eq. (12) equals zero. In other words,

$$1 + N(KG)_e = 0$$

$$(KG)_e = \frac{s}{[c_2]s^2 + [c_1 + b_0 K_s\{K_r G_i + K_d G_o\}]s + [c_0 + b_0 K_s\{G_i + K_p G_o\}]} \tag{13}$$

where $(KG)_e$ denotes the effective loop gain wrapped around the Coulomb friction element. Figure 7 shows the amplitude response of $-1/N$ superimposed on the frequency response of $(KG)_e$. The intersection indicates a limit cycling tendency with amplitude and frequency of

$$A_\theta = 0.178 \text{ deg}, \qquad \omega = 3.17 \text{ rad/s} \tag{14}$$

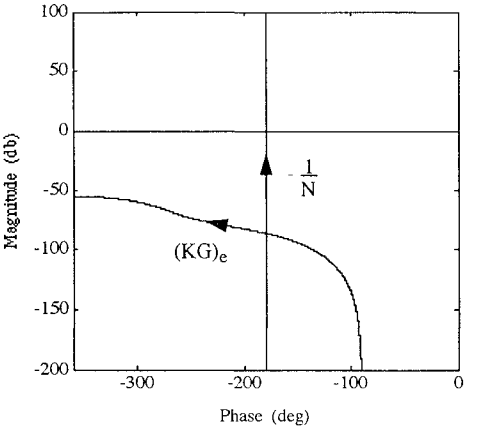

Fig. 7 Limit cycling solution using the Nichols chart.

From Fig. 1 near 70 s and the postflight analysis results,[3,4] the flight vehicle experienced oscillations of

$$A_\theta = 0.25 \text{ deg}, \qquad \omega = 2.1 \text{ rad/s} \tag{15}$$

which are in rough agreement with the predicted values considering the level of modeling used.

To assess the importance of the remnant, consider the attenuation effects of $(KG)_e$. With a limit cycle frequency of $\omega = 3.17$ rad/s, the lowest harmonic appearing in the remnant signal is $\omega = 9.51$ rad/s. Using Eq. (13), attenuation of the lowest harmonic remnant signal around the loop, relative to the fundamental amplitude, is 3, that is to say, amplification by a factor of 3, giving a net attenuation of $1/3 \times 3 = 1$. Here, the effect of the remnant on the input to the Coulomb friction element is indeed significant, and the predicted amplitude value should not be trusted. On the other hand, the predicted frequency value is not dependent on this effect due to the describing function's independence of frequency, i.e., the intersection location and frequency from Fig. 7 are unchanged as N varies in magnitude.

The exact limit cycling behavior (under the given models) can only be had from nonlinear simulation. Using the block diagrams in Figs. 2 and 5, the state variable and control law equations during dynamic motion are

$$\dot{z} = A_d z + f(z) + Bu$$

$$u = K_{u_c} u_c - K_z z$$

$$z = [\delta \quad \dot{\delta} \quad \theta \quad \dot{\theta} \quad x \quad \dot{x}]^T$$

$$f(z) = [0 \quad -B(\dot{\delta})/c_2 \quad 0 \quad 0 \quad 0 \quad 0]^T$$

$$u = \delta_c, \qquad u_c = x_c$$

$$A_d = \begin{bmatrix} 0 & 1 & 0 & 0 & 0 & 0 \\ -c_0/c_2 & -c_1/c_2 & 0 & 0 & 0 & 0 \\ 0 & 0 & 0 & 1 & 0 & 0 \\ (l_v T_v)/I_v & 0 & 0 & 0 & 0 & 0 \\ 0 & 0 & 0 & 0 & 0 & 1 \\ T_v/m_v & 0 & 0 & 0 & 0 & 0 \end{bmatrix} \tag{16}$$

$$B = [0 \quad b_0/c_2 \quad 0 \quad 0 \quad 0 \quad 0]^T \qquad K_{u_c} = K_s$$

$$K_z = K_s[0 \quad 0 \quad 1 \quad K_r \quad K_p \quad K_d]$$

During the static condition, the pertinent equations are

$$\dot{z} = A_s z$$
$$u = K_{u_c} u_c - K_z z \tag{17}$$

where A_s equals A_d with the second row replaced with all zeros. The logic for determining which condition is applicable is the following:

$$\text{if } \dot{\delta} = 0 \text{ and } |b_0\delta_c - c_0\delta| \le f, \text{ then static}$$
$$\text{if } \dot{\delta} \ne 0 \text{ or } |b_0\delta_c - c_0\delta| > f, \text{ then dynamic} \tag{18}$$

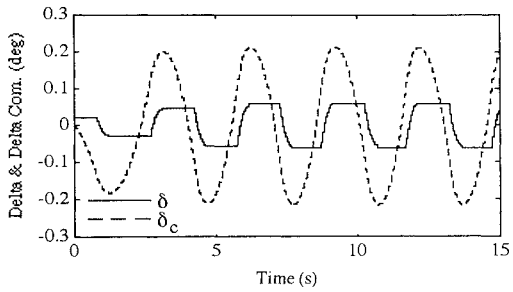

Fig. 8 Nozzle deflection response.

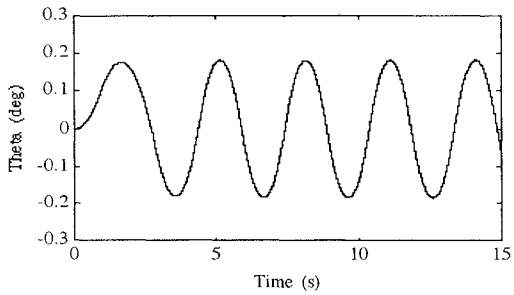

Fig. 9 Vehicle pitch attitude response.

Nozzle deflection and pitch angle responses are shown in Figs. 8 and 9 for an initial nozzle deflection of 0.02 deg and $x_c = 0$. Observe in Fig. 8 the sticking–unsticking behavior, both on a large and small scale. The long periods of sticking at the peak amplitude correspond to a reversal in the direction of the commanded actuator position. The short periods of sticking similar to a ratchet-type motion correspond to a unidirectional change in the commanded actuator position coupled with a highly responsive actuator-nozzle system.

From Fig. 9, the limit cycling amplitude and frequency are

$$A_\theta = 0.183 \text{ deg}, \qquad \omega = 2.10 \text{ rad/s} \tag{19}$$

Observe that both the predicted amplitude and frequency from simulation agree with the predicted values in Eq. (14), thus offering support to the describing function analysis. Unexpectedly, the amplitude value here agrees with the value predicted by the describing function analysis in Eq. (14), in spite of the error due to neglecting the remnant signal. Finally, the simulation results agree quite well with the observed values in Eq. (15).

Control of Limit Cycling Tendencies

Given that actuator and/or nozzle hardware changes are not feasible, attention is now focused on control system fixes to lessen the tendency to oscillate. These fixes should have minimal effect on the vehicle closed-loop stability and performance, or at least the flight control engineer should be abreast of the tradeoffs with stability and performance. An indirect scheme consisting of feedback gain adjustment will be considered first.

A closer examination of the Nichols chart in Fig. 7 and the expression for $(KG)_e$ in Eq. (13) indicates gain adjustment is a practical and effective means of lessening the limit cycling behavior. From Fig. 7, if the effective loop transfer $(KG)_e$ can be made to intersect the negative inverse of the describing function $-1/N$ at a lower magnitude value, then the limit cycle amplitude will decrease (since lower magnitude values for $-1/N$ correspond to lower input amplitudes).

Using the vehicle transfer functions in Eq. (1), $(KG)_e$ in Eq. (13) can be rewritten as

$$(KG)_e = \frac{s^3}{\underbrace{\{c_2s^2 + c_1s + c_0\}}_{\text{actuator-nozzle}} \underbrace{s^2 + b_0K_sT_v\left\{K_r\frac{l_v}{I_v} + K_d\frac{1}{m_v}\right\}s + b_0K_sT_v\left\{\frac{l_v}{I_v} + K_p\frac{1}{m_v}\right\}}_{\text{closed-loop vehicle}}} \tag{20}$$

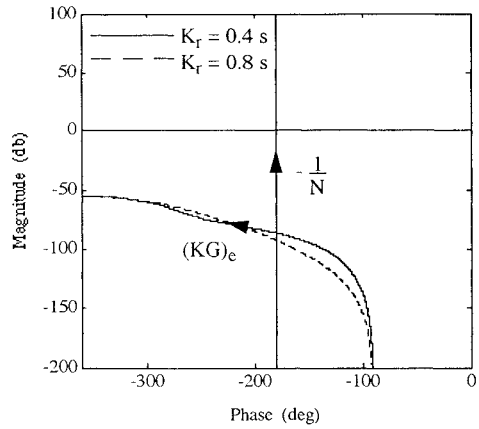

Fig. 10 Limit cycling solution with feedback gain adjustment.

Note the poles of $(KG)_e$ consist of two real, high-frequency, actuator-nozzle modes and a complex, lower frequency, closed-loop vehicle mode as approximately indicated in Eq. (20). From Eq. (20), also note that for frequencies below the closed-loop vehicle mode, $(KG)_e$ consists primarily of three differentiators divided by a gain. In Fig. 7, this structure corresponds to increasing magnitude at a constant phase of -90 deg. For higher frequencies, a 180-deg drop in phase is observed in Fig. 7 around -100 dB magnitude, corresponding to the closed-loop vehicle mode. In this region, the actuator-nozzle mode can be neglected.

With this insight, the intersection between $(KG)_e$ and $-1/N$ can be modified to a lower magnitude value by forcing the closed-loop vehicle phase rolloff to occur sooner. This effect precisely occurs when the closed-loop vehicle mode damping increases, which can be achieved by increasing either or both feedback gains K_r and K_d as seen from Eq. (20). Figure 10 shows the Nichols chart results for the original value of K_r and for double the original value. Observe how the phase rolloff occurs sooner, allowing an intersection at a lower magnitude value. The limit cycle amplitude and frequency for the new system are

$$A_\theta = 0.0895 \text{ deg}, \qquad \omega = 3.17 \text{ rad/s} \tag{21}$$

The oscillatory amplitude has been reduced from the original value in Eq. (14) by about half with no change in frequency.

Improved limit cycling characteristics by feedback gain adjustment do not come free, but rather at the expense of altering the vehicle closed-loop stability and performance. The loop transfer corresponding to δ in Fig. 2 can be written as

$$(KG)_\delta = \frac{K_sT_v}{s^2}\frac{b_0}{c_2s^2 + c_1s + c_0} \times \left\{\left[K_r\frac{l_v}{I_v} + K_d\frac{1}{m_v}\right]s + \left[\frac{l_v}{I_v} + K_p\frac{1}{m_v}\right]\right\} \tag{22}$$

and the corresponding Bode plot is shown in Figs. 11 and 12 for the original value of K_r and for the new value. Observe that after gain adjustment, the open-loop magnitude crossover has increased from 4.7 rad/s to 8.2 rad/s, indicating a beneficial effect on the closed-loop performance via a more responsive behavior and less overshoot. Also note from Figs. 11 and 12 that the phase margin has increased from 60 deg to 76 deg, whereas the gain margin has decreased from 44 dB to 38 dB. These observations indicate an adverse effect upon closed-loop stability robustness because, practically speaking, higher frequencies are where modeling uncertainties reside and also where the gain margin has dropped. Further, the increased open-loop

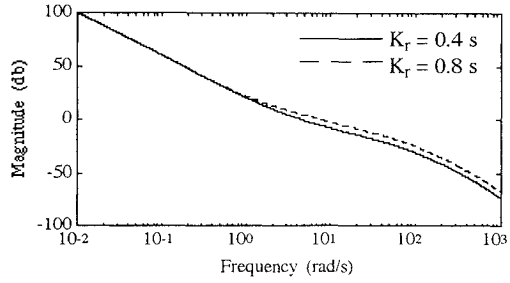

Fig. 11 Loop transfer magnitude at δ.

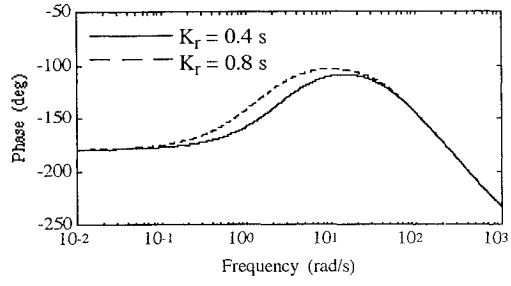

Fig. 12 Loop transfer phase at δ.

crossover will degrade the stability robustness since the phase in Fig. 12 can be expected to drop off much sooner in the region from 10 rad/s to 100 rad/s where hydraulic actuator flapper dynamics, vehicle structural modes, and control system filters and delays are located.

Lessening of the limit cycling behavior by feedback gain adjustment is only semieffective because of its inherently indirect approach and its impact on the vehicle closed-loop stability and performance. A more direct scheme, and hopefully more transparent to the closed-loop stability and performance characteristics, is now considered, using active control.

As discussed previously, the limit cycling behavior is due to nozzle sticking, especially during the longer periods as noted in Fig. 8 where the commanded position reverses direction. A control system that can unstick the nozzle earlier than the current feedback structure does, as well as drive the nozzle to stick nearer the commanded position, should lessen the limit cycling tendency. An impulsive control scheme suitable for accomplishing this task is addressed next.

Reconsider the governing differential equation for the nozzle motion in Eq. (6), or

$$c_2\ddot{\delta} + c_1\dot{\delta} + c_0\delta = b_0\delta_c' - f\,\mathrm{sgn}\{\dot{\delta}\} \tag{23}$$

where the new commanded signal δ_c' is given by the addition of the original nozzle command signal δ_c with an impulse.

$$\delta_c' = \delta_c + \tilde{\delta}_c\Delta(t - t_i) \tag{24}$$

In Eq. (24), $\tilde{\delta}_c$ represents the impulse magnitude, $\Delta(t - t_i)$ the Dirac delta function, and t_i the impulse application time. Recall that an impulse can be interpreted as an initial velocity,[13] or

$$\dot{\delta}(t_i^+) = \frac{\int_{t_i^-}^{t_i^+}\{b_0\tilde{\delta}_c\}\Delta(\tau - t_i)\,\mathrm{d}\tau}{c_2} = \frac{b_0\tilde{\delta}_c}{c_2} \tag{25}$$

where t_i^- and t_i^+ are times infinitesimally before and after the impulse, respectively. The $\dot{\delta}(t_i^+)$ and t_i are to be calculated next.

Starting from a static condition with $\delta \neq \delta_c$ and at time t_i, what initial velocity should be given to the nozzle so that after one-half cycle of motion with the command signal present, the nozzle position equals the commanded position and is static? To determine this value, the solution to Eq. (23) is invoked, or

$$\delta(t) = \{Ae^{\lambda_1(t-t_i)} + Be^{\lambda_2(t-t_i)}\}\delta(t_i) + C\{e^{\lambda_1(t-t_i)} - e^{\lambda_2(t-t_i)}\}\dot{\delta}(t_i^+) + \{De^{\lambda_1(t-t_i)} + Ee^{\lambda_2(t-t_i)} + F\} \times [b_0\delta_c - f\,\mathrm{sgn}\{\dot{\delta}(t_i^+)\}] \tag{26}$$

where δ_c has been assumed constant, $\lambda_{1,2}$ are the roots of the characteristic equation, and

$$A = \frac{c_2\lambda_1 + c_1}{c_2(\lambda_1 - \lambda_2)} \qquad B = \frac{c_2\lambda_2 + c_1}{c_2(\lambda_2 - \lambda_1)}$$
$$C = \frac{1}{\lambda_1 - \lambda_2}$$
$$D = \frac{1}{c_2\lambda_1(\lambda_1 - \lambda_2)} \qquad E = \frac{1}{c_2\lambda_2(\lambda_2 - \lambda_1)} \tag{27}$$
$$F = \frac{1}{c_2\lambda_1\lambda_2}$$

Solving for $\dot{\delta}(t_i^+)$ from Eq. (26) with $\delta(t) = \delta_c$ yields the desired initial velocity.

In solving for $\dot{\delta}(t_i^+)$, $\mathrm{sgn}\{\dot{\delta}(t_i^+)\}$ can be replaced in Eq. (26) by $\mathrm{sgn}\{\delta_c - \delta\}$ without any loss of generality when considering only one-half cycle of motion. Equation (25) can be used to determine the commanded nozzle impulse magnitude from $\dot{\delta}(t_i^+)$. Note the solution for the initial velocity explicitly involves the undetermined and unconstrained time to complete the half-cycle denoted as $t_{hc} = t - t_i$. A small value relative to the commanded nozzle position time constant can be selected and used as a design parameter. This selection will validate the assumption of a steady command signal during transient motion following an impulse.

The next consideration is determining when the impulse should be applied. A relative simple condition for determining the impulse time is when the error in the nozzle position exceeds a tolerance value denoted as ε_δ, or

$$t = t_i \qquad \text{when} \qquad |\delta_c - \delta| \geq \varepsilon_\delta \tag{28}$$

Here, ε_δ is also a design parameter and any small value, relative to the normalized friction value f/c_0 or f/b_0, should unstick the nozzle earlier than according to the torque condition in Eq. (18). To avoid the application of successive impulses at an impractical rate with regard to hardware limitations, or simply to slow the system down, the impulse is not applied until a second condition is also satisfied. The second condition is that the elapsed time since the current static condition commenced must exceed a tolerance value ε_t, or

$$t = t_i \quad \text{when} \quad |\delta_c - \delta| \geq \varepsilon_\delta \quad \text{and} \quad |t - t_{\text{stick}}| \geq \varepsilon_t \tag{29}$$

with t_{stick} denoting the time at sticking. The value ε_t can be thought of as another design parameter.

The impulsive control scheme is illustrated in Fig. 13 and using Eq. (24)

$$f(\delta, \dot{\delta}, \delta_c) = \tilde{\delta}_c\Delta(t - t_i) \tag{30}$$

Observe that the impulsive control scheme is simply imbedded into the existing vehicle control system and consists of an additional feedback loop around the actuator-nozzle system along with a feedforward path. The $\dot{\delta}$ feedback signal is only for determination of a static condition. These additional feedback signals require two extra sensors which are not present in the original hardware in Figs. 3 and 4. Note that impulses do not occur until after the nozzle becomes stuck. Also note that the static and dynamic conditions based on torque in Eq. (18) are also still in effect.

A simulation of the complete control system indicated in Fig. 13 for the same initial condition as that used to generate Figs. 8 and 9

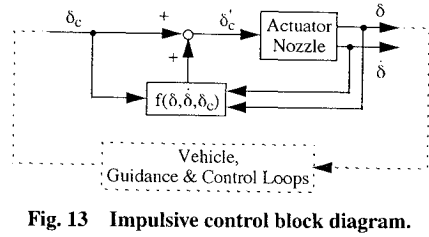

Fig. 13 Impulsive control block diagram.

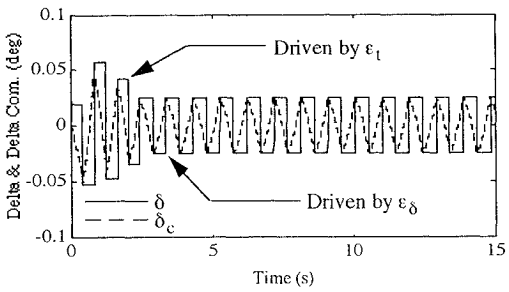

Fig. 14 Nozzle deflection response using impulsive control.

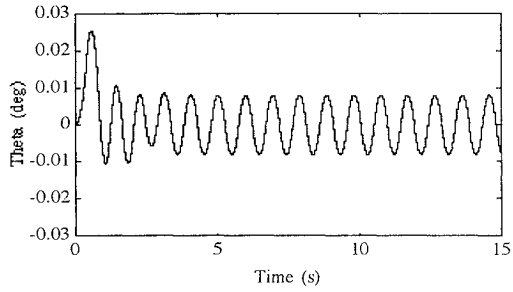

Fig. 15 Vehicle pitch attitude response using impulsive control.

has been conducted. The following numerical values were used for the impulsive control design parameters:

$$t_{hc} = 0.002 \text{ s}, \qquad \varepsilon_\delta = 0.05 \text{ deg}, \qquad \varepsilon_t = 0.4 \text{ s} \tag{31}$$

Figures 14 and 15 show the nozzle deflection and pitch angle responses. Observe in Fig. 14 the sticking-unsticking behavior. Here, the short periods of sticking or the ratchet type motion has been eliminated with the impulsive control logic. Below 2.5 s, impulses occur every 0.4 s, indicating the elapsed time tolerance is driving the impulses. On the other hand, above 2.5 s note the change in frequency of the applied impulses, indicating the nozzle error tolerance is driving the impulses. From Fig. 15, the limit cycling amplitude and frequency are

$$A_\theta = 0.00817 \text{ deg}, \qquad \omega = 6.59 \text{ rad/s} \tag{32}$$

indicating the impulsive logic is effectively controlling the limit cycling behavior relative to the original or gain adjusted systems in Eqs. (19) and (21). Note the improvement has been achieved with smaller nozzle deflections but higher bandwidth.

To assess the robustness of the control system to parameter uncertainty in the impulsive control law, two additional simulations are considered. The uncertainty considered is the Coulomb friction value f used in the calculation of $\dot{\delta}(t_i^+)$ in Eq. (26). Half and double the true value of $f = 137.5$ lbf ft in Eq. (7) are considered. Figures 16–19 show the nozzle and pitch angle responses.

In the underestimated case in Figs. 16 and 17, the nozzle consistently undershoots the desired position. Observe the loss of symmetry in both responses about zero. Further, note the nozzle and elapsed time tolerances alternate in driving the impulses. The amplitude (one-half of peak to peak) and frequency values from Fig. 17 are

$$A_\theta = 0.0132 \text{ deg}, \qquad \omega = 4.60 \text{ rad/s} \tag{33}$$

implying stability and performance robustness since the impulsive logic remains effective in controlling the limit cycling behavior.

In the overestimated case in Figs. 18 and 19, the nozzle consistently overshoots the desired position. From Fig. 18, note the elapsed time tolerance and the torque condition in Eq. (18) alternate in driving the nozzle from the static condition. The amplitude and frequency values from Fig. 19 are

$$A_\theta = 0.184 \text{ deg}, \qquad \omega = 2.80 \text{ rad/s} \tag{34}$$

Even though the parameter uncertainty resulted in the impulsive control law being bypassed roughly half of the time by reintroducing

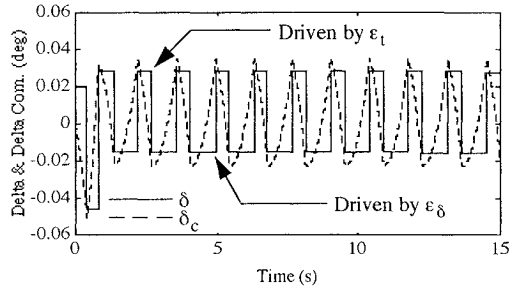

Fig. 16 Nozzle deflection response using impulsive control and $\frac{1}{2}f$.

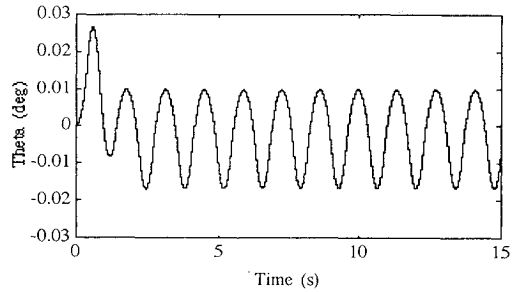

Fig. 17 Vehicle pitch attitude response using impulsive control and $\frac{1}{2}f$.

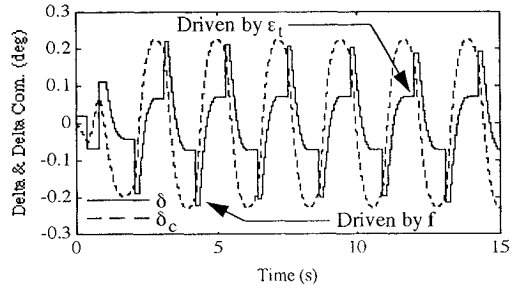

Fig. 18 Nozzle deflection response using impulsive control and $2f$.

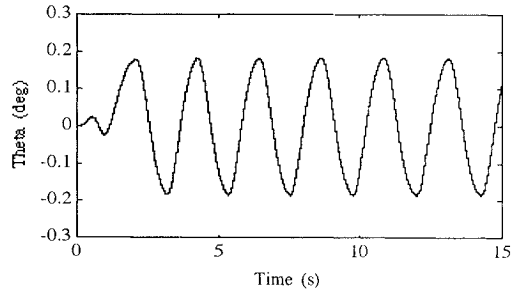

Fig. 19 Vehicle pitch attitude response using impulsive control and $2f$.

the torque condition in Eq. (18), a certain level of robustness is indicated by the vehicle pitch amplitudes returning to approximately the level observed for the original system in Eq. (19).

The preceding impulsive control analysis is by no means complete. The ability of the actuator to supply an impulse under bandwidth and rate limit restrictions is of concern. Resolution of the nozzle rate sensor to detect a static condition is also of concern. Further, excitation of vehicle structural modes with impulses must be assessed. Finally, how does the impulsive control logic behave under different dynamic conditions such as forced vehicle motion?

Conclusions

The results presented here strongly support the suspicion that observed in-flight oscillations are indeed limit cycling due to the presence of Coulomb friction in the nozzle pivot. Further, the results alleviate concerns that the oscillations are due to a control system design flaw that could possibly lead to unstable motions. Although not discussed, the limit cycle results indicate stable characteristics,

further boosting confidence in the control system design. Both feedback gain adjustment and active control, rooted in classical linear systems theory and control theory, appear to be effective in reducing the inherent limit cycling tendencies. However, a design tradeoff with closed-loop stability and performance is present with these methods.

Acknowledgments

This work was partially performed under USASDC Contract DASG60-89-C-0091. This support is appreciated. Assistance from Bruce Bollermann, Paul Kunz, Chen Kuo, Jim Reich, Dean Zes, and Harry Blackiston is also greatly appreciated.

References

[1]Lenorovitz, J. M., "Funding Pits Patriot, ERINT in TBM Defense Upgrade Contest," *Aviation Week and Space Technology*, Vol. 138, No. 2, 1993, pp. 22, 23.

[2]Lenorovitz, J. M., "Pegasus Lofts Brazil's SCD1," *Aviation Week and Space Technology*, Vol. 138, No. 7, 1993, pp. 64, 65.

[3]Kunz, P., "ERINT Target System Demonstration Post Flight Report," Orbital Sciences Corp., SDD TM-8931, Space Data Div., March 1992.

[4]Kunz, P., "Ballistic Tactical Target Vehicle (BTTV) Demo II Post Flight Report," Orbital Sciences Corp., SDD TM-9693, Space Data Div., Nov. 1992.

[5]Newman, B., "Prediction and Control of Limit Cycling Motions in Boosting Rockets," *Proceedings of the AIAA Guidance, Navigation, and Control Conference* (Monterey, CA), AIAA, Washington, DC, 1993, pp. 1658–1667.

[6]Kunz, P., "ERINT Target System Guidance and Control System Analysis and Design Document," Orbital Sciences Corp., SDD TM-8592, Space Data Div., March 1992.

[7]Newman, B., "Limit Cycling Prediction for Missions Employing Minuteman Stage 3 Hardware," Orbital Sciences Corp., SDD TM-10042, Space Data Div., Nov. 1992.

[8]Burton, E. R., "Model Specification Control, Exhaust Nozzle C-4035/DJW-15 (Model P72B)," Autonetics, S-133-1004-15, March 1962.

[9]Burton, E. R., "Minuteman Data Book Section 6.0, Issue No. 6, Guidance and Control (WS-133B Data Book)," Autonetics, 7550-T439-L4-00, Jan. 1966.

[10]Blackiston, H., Private communications, TRW Space Park, June 1992.

[11]Newman, B., "Measurements of Minuteman I Stage 3 Hardware Conducted at Orbital Sciences Corporation, Space Data Division," Orbital Science Corp., Space Data Div., Sept. 1992.

[12]Graham, D., and McRuer, D., *Analysis of Nonlinear Control Systems*, Wiley, New York, 1961.

[13]Meirovitch, L., *Elements of Vibration Analysis*, McGraw–Hill, New York, 1975.

[14]Haas, V. B., "Coulomb Friction in Feedback Control Systems," *Transactions of the American Institute of Electrical Engineers*, Vol. 72, Pt. II, 1953, pp. 119–126.

[15]McCann, G. D., Lindvall, F. C., and Wilts, C. H., "The Effect of Coulomb Friction on the Performance of Servomechanisms," *Transactions of the American Institute of Electrical Engineers*, Vol. 67, Pt. I, 1948, pp. 540–546.

[16]Graham, D., and McRuer, D., "Retrospective Essay on Nonlinearities in Aircraft Flight Control," *Journal of Guidance, Control, and Dynamics*, Vol. 14, No. 6, 1991, pp. 1089–1099.